Task-based optimization and performance assessment in optical coherence imaging

Jannick Rolland, Jason O'Daniel, Ceyhun Akcay, Tony DeLemos, and Kye S. Lee

College of Optics and Photonics: CREOL & FPCE, University of Central Florida, Orlando, Florida 32816

Kit-Iu Cheong and Eric Clarkson

Optical Sciences Center and Department of Radiology, University of Arizona, Tucson, Arizona 85720

Ratna Chakrabarti

Molecular Biology and Microbiology Department, University of Central Florida, Orlando, Florida 32816

Robert Ferris

University of Pittsburgh Cancer Institute, Pittsburgh, Pennsylvania 15215

Received July 8, 2004; revised manuscript received October 12, 2004; accepted December 1, 2004

Optimization of an optical coherence imaging (OCI) system on the basis of task performance is a challenging undertaking. We present a mathematical framework based on task performance that uses statistical decision theory for the optimization and assessment of such a system. Specifically, we apply the framework to a relatively simple OCI system combined with a specimen model for a detection task and a resolution task. We consider three theoretical Gaussian sources of coherence lengths of 2, 20, and 40 μm. For each of these coherence lengths we establish a benchmark performance that specifies the smallest change in index of refraction that can be detected by the system. We also quantify the dependence of the resolution performance on the specimen model being imaged. © 2005 Optical Society of America

OCIS codes: 000.5490, 030.6600, 170.4500.

1. INTRODUCTION

Optical coherence imaging (OCI), which encompasses optical coherence tomography and optical coherence microscopy, is an interferometric technique using the low coherence property of light to axially image at high resolution in biological tissues.[1–3] While the concept of OCI is relatively simple to understand, the instrumentation and optimization of an OCI system is a challenging undertaking. This challenge in developing an OCI system includes considerations such as the properties of the light source, possible modulation, polarization dependence, component dispersion, and the tissue type being imaged. In addition, this difficulty is compounded by the fact that a single OCI system may not necessarily be optimized for every task that may be presented. Using the method of trial and error to optimize an OCI system would take an inordinate amount of time. Therefore a mathematical method for task-based optimization and performance assessment of an OCI system incorporating the above-mentioned considerations would be an extremely useful technique. Such an optimization and performance assessment of an OCI system can be constructed on the basis of task performance by using statistical decision theory.

In statistical decision theory, there are two types of tasks that can be performed: estimation and classification. In estimation tasks, a parameter is inferred from the data given. A radiologist required to provide the approximate size of a tumor given an image of the tumor is an example of an estimation task. In a classification task, the data given are inferred to belong to a given set of classes. A radiologist required to determine whether an image does or does not contain a tumor is an example of a classification task. Any task that consists of only two possible hypotheses is known as a binary classification task. In this paper we will be concerned only with binary classification tasks; the specific tasks with which we are concerned will be detailed in Section 3. In general, binary classification operates on two hypotheses: The first is known as the negative hypothesis H_0; the second is known as the positive hypothesis H_1. If the negative hypothesis is true, the data to be classified belong to the zeroth class. Similarly, if the positive hypothesis is true, the data to be classified belong to the first class.

Regardless of whether the task is an estimation or a classification task, an observer will be present. An observer is defined as the means by which a task is accomplished, whether this observer is a person or a machine.[4] Several types of observer models for binary decision tasks can be found in the literature.[5–8] The pinnacle of observer models, against which all other observers can be compared, is the ideal observer. The ideal observer is an observer that uses all statistical information available to maximize task performance. However, this observer requires full knowledge of the probability density functions

of the data under each hypothesis. Therefore as the complexity of the OCI system increases, the ideal observer quickly becomes intractable. Hence a less-demanding observer must be considered. A linear model or linear discriminant presents a fine option because linear discriminants are easy to compute, the performance is easy to summarize, and far less information is needed on the data statistics than is needed by the ideal observer. The optimal linear discriminant is the Hotelling observer,[4] which we will adopt in this paper. The ability of the Hotelling observer to discriminate between the data belonging to the class associated with the negative or the positive hypothesis is represented by a scalar quantity known as the detectability index.

We propose to use the detectability index to determine how to optimize an OCI system or determine how well an OCI system performs for a given task. The detectability index is the effective signal-to-noise ratio associated with a measured area under the receiver operator characteristic curve (AUC), which is a measure of the average of the true positive fraction, for all values of the false positive fraction. The true positive fraction is the ratio of correct decisions for the positive hypothesis to the total number of cases in which the positive hypothesis is true. The false positive fraction is the ratio of incorrect decisions for the positive hypothesis to the total number of cases in which the negative hypothesis is true. A more detailed explanation of the detectability, the receiver operator characteristic curve, the AUC, the true positive fraction and the false positive fraction is given by Barrett and Myers.[4]

These scalar quantities known as the detectability and the AUC depend on the entire OCI system setup as well as on the specimen being imaged. Therefore in modeling the entire OCI system, which includes a specimen model, the system can be optimized by varying one of its parameters and investigating the effect on the detectability index and the AUC. Also, by varying the parameters of the specimen model, the diagnostic performance of the system may also be assessed.

In order to evaluate an OCI system for specific tasks, we must know how the detectability index and the AUC are defined mathematically as they relate to the OCI system and how the specimen model being imaged and the specific tasks are defined. These three subjects are treated in Section 2. If we consider a simple OCI system, a benchmark performance can be established. In the future, when complexity is added to the system, this benchmark performance will provide a standard to which these more complex systems may be compared. Therefore in Section 3 we define a simple OCI system and apply the mathematics presented in Section 2 to the simple OCI system for the defined tasks for the purpose of performance assessment. In this assessment we investigate three theoretical sources with Gaussian power spectral densities (PSDs) of various spectral widths. We choose the three different spectral widths in order to approximate the various spectral widths currently available in OCI. In Section 4 we verify that the results of these simulations behave as expected, present the benchmark performance found, and reiterate the assumptions used and possible extensions of the work presented. Finally, Section 5 provides a short summary of the work.

2. METHODS

In this section the expressions for the detectability index and the AUC will be reviewed, and their application to a general OCI system will be provided. Also, the specimen model being imaged will be described, and the tasks will be defined.

A. Detectability Index and Area under the Receiver Operator Characteristic Curve

From statistical decision theory, the detectability index for a binary classification task associated with the Hotelling observer based on discrete measures is given by[9]

$$d^2 = \mathbf{X}^\dagger \mathbf{K}^{-1} \mathbf{X}. \tag{1}$$

The quantity $\mathbf{X}$ is an $N \times 1$ column vector representing the difference between the ensemble averages of members of each of the two classes of the binary classification task. Specifically, we have two classes, the zeroth class and the first class, as previously stated. Also let us assume that we have a system output depending on time, denoted $I(t)$. Given that the H_0 hypothesis is correct, an output $I_0(t)$ will be present (i.e., the zeroth class is present); or if the H_1 hypothesis is correct, an output $I_1(t)$ will be present (i.e., the first class is present). Each of these two outputs, $I_0(t)$ and $I_1(t)$ will have an associated noise. Therefore over an ensemble of these outputs the averages of these outputs will be $\langle\langle I_0(t)\rangle\rangle$ and $\langle\langle I_1(t)\rangle\rangle$, where $\langle\langle\cdot\rangle\rangle$ denotes the ensemble average or the statistical average over the two sources of randomness that we will consider. The inner angle bracket will represent an average over the Poisson noise at the detector that is conditional on the source field. The outer bracket will indicate the average over the Gaussian statistics of the source field. Occasionally we will use a single set of angle brackets when we are averaging over the source statistics only. This will occur when the quantity being averaged is a deterministic function of the source field either by definition or because the Poisson statistics have already been averaged out. These averages are sampled at discrete points in time, and the elements of the $\mathbf{X}$ vector are given as

$$X_n = \langle\langle I_1(t_n)\rangle\rangle - \langle\langle I_0(t_n)\rangle\rangle. \tag{2}$$

The quantity $\mathbf{K}$ in Eq. (1) is an $N \times N$ matrix representing the weighted average, depending on the *a priori* probability of each class, of the autocovariance matrices of each of the two classes. The autocovariance matrix or sampled data can be computed from sampling of the autocovariance function or from the continuous process. For a given class, the ith class ($i = 0, 1$), for instance, the autocovariance function, will be given by

$$K_i(t,t') = \langle\langle I_i(t) I_i(t')\rangle\rangle - \langle\langle I_i(t)\rangle\rangle\langle\langle I_i(t')\rangle\rangle. \tag{3}$$

When the autocovariance function for each class is sampled at discrete points in time, the elements of the $\mathbf{K}$ matrix are given by

$$K_{nm} = p(H_0) K_0(t_n, t_m) + p(H_1) K_1(t_n, t_m), \tag{4}$$

where $p(H_0)$ and $p(H_1)$ are the *a priori* probabilities of hypotheses H_0 and H_1, respectively, being true. If we assume that each class has an equal probability of occurring, Eq. (4) becomes

$$K_{nm} = \tfrac{1}{2}K_0(t_n,t_m) + \tfrac{1}{2}K_1(t_n,t_m). \quad (5)$$

The way that the detectability index is best related to diagnosis is through the AUC. Assuming that the distribution of the Hotelling test statistic is normal under both the zeroth class and the first class, the AUC may be expressed in terms of the detectability as[4]

$$\mathrm{AUC} = \tfrac{1}{2} + \tfrac{1}{2}\,\mathrm{erf}(\sqrt{d^2}/2). \quad (6)$$

This normality assumption can be justified under the central-limit theorem since the Hotelling test statistic is a linear combination of the components of the data vector and, for the SKE task we are considering, these components are statistically independent random variables.

B. Required Quantities of the Optical Coherence Imaging System

The basic OCI system is quite simple in construction; an example is the free-space OCI system shown in Fig. 1. Generally, the measured output of an OCI system is directly related to the detected photocurrent. Therefore we will let this detected photocurrent be our OCI system output $I(t)$. To compute the detectability as given in (1), we must first derive the photocurrent $I(t)$ along with its mean $\langle\langle I(t)\rangle\rangle$ and its autocovariance function $K(t,t')$. Both the mean photocurrent data and the autocovariance function of the photocurrent data are derived for the case of unpolarized light, isotropic propagation through the system, and only normal incidence of the light propagating through the system. The mean photocurrent and autocovariance function can be extended past this simple case so that polarization and nonnormal incidence may be taken into account; however, within the scope of this paper the simple case will be considered to establish a benchmark performance. Our strategy in what follows is to show how we may express the mean and the autocovariance functions of the photocurrent data, and we will discover in the process that certain statistical moments of the source are needed. We will express these moments, in terms of the spectral characteristics of the source, as they arise.

The photocurrent from the detector can be expressed simply as the number of photoelectrons $N(t)$ created as a function of time by the incident electric field as

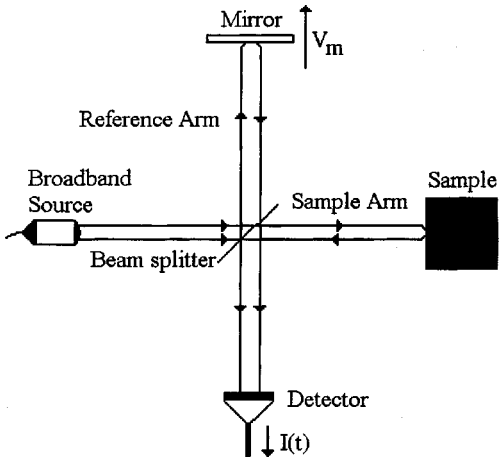

Fig. 1. Basic free-space OCI system setup.

$$I(t) = \frac{e}{\Delta t}\int_{t-\Delta t}^{t} N(t')\mathrm{d}t', \quad (7)$$

where e is the charge of an electron (1.6×10^{-19} C) and Δt is the integration window associated with the detector. For the sake of simplicity, we can rewrite the photocurrent from Eq. (7) as

$$I(t) = \frac{e}{\Delta t}\int_{-\infty}^{\infty} r(t-t')N(t')\mathrm{d}t', \quad (8)$$

where the function $r(t)$ is defined as

$$r(t) = \begin{cases} 1 & 0 \leqslant t \leqslant \Delta t \\ 0 & \text{otherwise} \end{cases}. \quad (9)$$

The number of photoelectrons created is directly proportional to the electric field incident on the detector, which is proportional to the electric field emitted from the source. However, the electric field emitted from the broadband source and the creation of photoelectrons in the detection process have certain statistics associated with them. The broadband nature of the source ensures that the electric field emitted from the source will obey circular Gaussian statistics; also, it is well known that the creation of photoelectrons in the detection process obeys Poisson statistics.[10] Hence $N(t)$ may be referred to as a doubly stochastic Poisson random process.[4,10] We will now look at the statistics of the source and the detection process and investigate how these noise components contribute to the mean photocurrent. Within the scope of this paper we will not consider any other noise components.

1. Mean Photocurrent

To determine the mean photocurrent of the system, we must first look at the system input, the light source, and propagate this input through the system in order to determine the mean output. The light source emits an electric field $\mathbf{E}_s(t)$ that we can decompose into a superposition of plane waves by taking its Fourier transform and expressing it as

$$\mathbf{E}_s(t) = \int_{-\infty}^{\infty} \exp(i\omega t)\hat{\mathbf{E}}_s(\omega)\mathrm{d}\omega, \quad (10)$$

where the caret denotes a function in the Fourier domain. The amplitude of these plane waves will be split at the beam splitter. One part of the field will propagate through the reference arm. Through this propagation it will experience a phase delay $\phi_1(\omega,t)$, which will account for the optical path length, dispersion, modulation, and other possible phase delays in the reference arm. This part of the field will also experience a loss of amplitude and possibly phase shifts upon reflection, which will be described by $\hat{\alpha}(\omega)$; $\hat{\alpha}(\omega)$ will account for absorption and nonequal reflection amplitudes within the reference arm as well as incorporate losses due to the beam splitter. Another part of the field will propagate through the specimen arm. Through this propagation it will experience a phase delay $\phi_2(\omega,t)$, which will account for the optical path length, dispersion, modulation, and other possible phase delays in the specimen arm. This part of the field will also experience a loss of amplitude and phase shifts from the speci-

men model, described mathematically by $\hat{\beta}(\omega)$; $\hat{\beta}(\omega)$ will account for absorption, nonequal reflection amplitudes, and phase shift upon reflection due to the specimen model as well as incorporate losses due to the beam splitter. These altered parts of the field will recombine at the beam splitter, and part of this sum of fields will propagate to the detector; the remaining part of the sum will propagate back toward the source. Therefore the total electric field at the detector may be related to the electric field at the source by

$$\mathbf{E}(t) = \int_{-\infty}^{\infty} \{\hat{\alpha}(\omega)\exp[i\phi_1(\omega,t) + i\omega t] + \hat{\beta}(\omega)\exp[i\phi_2(\omega,t) + i\omega t]\}\hat{\mathbf{E}}_s(\omega)\mathrm{d}\omega. \quad (11)$$

For simplicity, hereafter we define

$$m(\omega,t) = \hat{\alpha}(\omega)\exp[i\phi_1(\omega,t)] + \hat{\beta}(\omega)\exp[i\phi_2(\omega,t)]. \quad (12)$$

Therefore Eq. (11) may be rewritten as

$$\mathbf{E}(t) = \int_{-\infty}^{\infty} m(\omega,t)\exp(i\omega t)\hat{\mathbf{E}}_s(\omega)\mathrm{d}\omega. \quad (13)$$

In Eq. (13) both $\mathbf{E}(t)$ and $\hat{\mathbf{E}}_s(\omega)$ are stochastic processes. Given that the source field $\mathbf{E}_s(t)$ obeys circular Gaussian statistics, $\langle \mathbf{E}_s(t)\rangle$ is zero. This implies that $\mathbf{E}(t)$ is also a Gaussian random process with $\langle \mathbf{E}(t)\rangle$ equal to zero.

Taking the statistical average over all random processes, Eq. (8) may be rewritten to give the mean photocurrent as

$$\langle\langle I(t)\rangle\rangle = \left\langle\left\langle \frac{e}{\Delta t}\int_{-\infty}^{\infty} r(t-t')N(t')\mathrm{d}t' \right\rangle\right\rangle = \frac{e}{\Delta t}\int_{-\infty}^{\infty} r(t-t')\langle\langle N(t')\rangle\rangle \mathrm{d}t'. \quad (14)$$

Noting again that $N(t)$ is a doubly stochastic Poisson random process, the conditional mean of $N(t)$ is given by

$$\bar{N}(t) = \frac{RA}{e\eta_0}\mathbf{E}^{\dagger}(t)\mathbf{E}(t) = \rho\mathbf{E}^{\dagger}(t)\mathbf{E}(t), \quad (15)$$

where R is the responsivity of the detector, A is the area of the detector, and η_0 is the impedance of free space (377 Ω). The quantity ρ is defined as

$$\rho = \frac{RA}{e\eta_0}. \quad (16)$$

From the conditional mean, the overall mean of the output is written as

$$\langle\langle N(t)\rangle\rangle = \langle\bar{N}(t)\rangle = \rho\langle\mathbf{E}^{\dagger}(t)\mathbf{E}(t)\rangle. \quad (17)$$

In Eq. (17), $\langle\langle N(t)\rangle\rangle$ is the average of $N(t)$ over the Poisson noise associated with detection and the Gaussian noise associated with the source field. On the other hand, $\langle\bar{N}(t)\rangle$ averages $\bar{N}(t)$ over the Gaussian statistics only, since the Poisson noise has already been averaged out to get $\bar{N}(t)$. If we combine Eqs. (13) and (17), $\langle\langle N(t)\rangle\rangle$ can be rewritten as

$$\langle\langle N(t)\rangle\rangle = \rho\int_{-\infty}^{\infty}\int_{-\infty}^{\infty} m^*(\omega,t)m(\omega',t)\exp[i(\omega'-\omega)t] \times \langle\hat{\mathbf{E}}_s^{\dagger}(\omega)\hat{\mathbf{E}}_s(\omega')\rangle \mathrm{d}\omega\mathrm{d}\omega'. \quad (18)$$

We will assume that the source field is a stationary random process and define the scalar autocovariance function of the source field as

$$G(\tau) = \langle\mathbf{E}_s^{\dagger}(t-\tau)\mathbf{E}_s(t)\rangle. \quad (19)$$

The stationarity assumption is related to the stability of the source. We may relax this assumption to quasi-stationarity in order to account for other sources of variation in the source field.[4] The scalar autocovariance function has the property

$$G^*(\tau) = G(-\tau). \quad (20)$$

This property ensures that the Fourier transform $\hat{G}(\omega)$ is real. Hereafter, $\hat{G}(\omega)$ will be denoted $S(\omega)$ to represent the PSD of the source.

The expectation $\langle\hat{\mathbf{E}}_s^{\dagger}(\omega)\hat{\mathbf{E}}_s(\omega')\rangle$ from Eq. (18) may be expressed by means of the inverse Fourier transform as

$$\begin{aligned}\langle\hat{\mathbf{E}}_s^{\dagger}(\omega)\hat{\mathbf{E}}_s(\omega')\rangle &= \frac{1}{4\pi^2}\int_{-\infty}^{\infty}\int_{-\infty}^{\infty}\exp[i(\omega' t_2 - \omega t_1)] \times \langle\mathbf{E}_s^{\dagger}(t_1)\mathbf{E}_s(t_2)\rangle \mathrm{d}t_1\mathrm{d}t_2 \\ &= \frac{1}{4\pi^2}\int_{-\infty}^{\infty}\int_{-\infty}^{\infty}\exp[i(\omega' t_2 - \omega t_1)] \times G(t_2 - t_1)\mathrm{d}t_1\mathrm{d}t_2 \\ &= \frac{1}{2\pi}\delta(\omega'-\omega)\int_{-\infty}^{\infty}\exp\left[i\left(\frac{\omega'+\omega}{2}\right)s\right]G(s)\mathrm{d}s \\ &= \delta(\omega'-\omega)S(\omega). \end{aligned} \quad (21)$$

Inserting Eq. (21) into Eq. (18), we rewrite $\langle\langle N(t)\rangle\rangle$ as

$$\langle\langle N(t)\rangle\rangle = \rho\int_{-\infty}^{\infty}|m(\omega,t)|^2 S(\omega)\mathrm{d}\omega. \quad (22)$$

Finally, the mean photocurrent can be expressed as

$$\langle\langle I(t)\rangle\rangle = \frac{\rho e}{\Delta t}\int_{-\infty}^{\infty} r(t-t')\left[\int_{-\infty}^{\infty}|m(\omega,t)|^2 S(\omega)\mathrm{d}\omega\right]\mathrm{d}t'. \quad (23)$$

2. Autocovariance Function of the Photocurrent

Now that we have an expression for the mean photocurrent, we next need the autocovariance function of the photocurrent in order to compute the detectability index. Starting with the autocovariance function expressed in Eq. (3) and substituting into it the expression in Eq. (8) for the various photocurrents, we can write the autocovariance function as

$$K(t,t') = \left(\frac{e}{\Delta t}\right)^2 \int_{-\infty}^{\infty}\int_{-\infty}^{\infty} r(t-t_1)r(t'-t_2)K_N(t_1,t_2)\mathrm{d}t_1\mathrm{d}t_2, \tag{24}$$

where $K_N(t_1,t_2)$ is the autocovariance function of the random process $N(t)$. This autocovariance function is expressed as

$$\begin{aligned} K_N(t_1,t_2) &= \langle\langle N(t_1)N(t_2)\rangle\rangle - \langle\langle N(t_1)\rangle\rangle\langle\langle N(t_2)\rangle\rangle \\ &= \langle\langle N(t_1)\rangle\rangle\delta(t_1-t_2) + K_{\bar{N}}(t_1,t_2). \end{aligned} \tag{25}$$

The term $K_{\bar{N}}(t_1,t_2)$ is the conditional autocovariance function, meaning that the Poisson statistics of the detection process are taken care of in the preceding term. This conditional autocovariance function is given by[4]

$$K_{\bar{N}}(t_1,t_2) = \langle\bar{N}(t_1)\bar{N}(t_2)\rangle - \langle\bar{N}(t_1)\rangle\langle\bar{N}(t_2)\rangle. \tag{26}$$

The first term on the right-hand side of Eq. (26) can be expressed in terms of the statistical properties of the field as

$$\begin{aligned} \langle\bar{N}(t_1)\bar{N}(t_2)\rangle &= \rho^2\langle\mathbf{E}^\dagger(t_1)\mathbf{E}(t_1)\mathbf{E}^\dagger(t_2)\mathbf{E}(t_2)\rangle \\ &= \rho^2\langle\mathbf{E}^\dagger(t_1)\mathbf{E}(t_1)\rangle\langle\mathbf{E}^\dagger(t_2)\mathbf{E}(t_2)\rangle \\ &\quad + \rho^2\,\mathrm{tr}[\langle\mathbf{E}(t_1)\mathbf{E}^\dagger(t_2)\rangle\langle\mathbf{E}(t_2)\mathbf{E}^\dagger(t_1)\rangle] \\ &= \langle\bar{N}(t_1)\rangle\langle\bar{N}(t_2)\rangle + \rho^2\,\mathrm{tr}[\langle\mathbf{E}(t_1)\mathbf{E}^\dagger(t_2)\rangle \\ &\quad \times\langle\mathbf{E}(t_2)\mathbf{E}^\dagger(t_1)\rangle], \end{aligned} \tag{27}$$

where tr is the three-dimensional trace function. Combining Eqs. (26) and (27), we can rewrite the conditional autocovariance function as

$$\begin{aligned} K_{\bar{N}}(t_1,t_2) &= \rho^2\,\mathrm{tr}[\langle\mathbf{E}(t_1)\mathbf{E}^\dagger(t_2)\rangle\langle\mathbf{E}(t_2)\mathbf{E}^\dagger(t_1)\rangle] \\ &= \rho^2\,\mathrm{tr}[\mathbf{J}(t_1,t_2)\mathbf{J}(t_2,t_1)] = \rho^2\,\mathrm{tr}[\mathbf{J}(t_1,t_2)\mathbf{J}^\dagger(t_1,t_2)], \end{aligned} \tag{28}$$

where

$$\mathbf{J}(t_1,t_2) = \langle\mathbf{E}(t_1)\mathbf{E}^\dagger(t_2)\rangle. \tag{29}$$

Now that we have the conditional autocovariance function in terms of the field at the detector, we can express it in terms of the field at the source. We define the autocovariance matrix of the source as

$$\mathbf{G}(\tau) = \langle\mathbf{E}_s(t)\mathbf{E}_s^\dagger(t-\tau)\rangle. \tag{30}$$

This matrix has the following two properties:

$$\mathbf{G}^\dagger(\tau) = \mathbf{G}(-\tau), \tag{31}$$

$$G(\tau) = \mathrm{tr}[\mathbf{G}(\tau)]. \tag{32}$$

Next, $\mathbf{J}(t_1,t_2)$ is computed as

$$\begin{aligned} \mathbf{J}(t_1,t_2) = \int_{-\infty}^{\infty}\int_{-\infty}^{\infty} & m(\omega,t_1)m^*(\omega',t_2)\exp[i(\omega t_1-\omega' t_2)] \\ & \times\langle\hat{\mathbf{E}}_s(\omega)\hat{\mathbf{E}}_s^\dagger(\omega')\rangle\mathrm{d}\omega\mathrm{d}\omega'. \end{aligned} \tag{33}$$

The expectation $\langle\hat{\mathbf{E}}_s(\omega)\hat{\mathbf{E}}_s^\dagger(\omega')\rangle$ from Eq. (33) may be expressed by means of the inverse Fourier transform, following the same scheme as in Eq. (21), as

$$\langle\hat{\mathbf{E}}_s(\omega)\hat{\mathbf{E}}_s^\dagger(\omega')\rangle = \delta(\omega'-\omega)\hat{\mathbf{G}}(\omega). \tag{34}$$

Combining Eqs. (28), (33), and (34) produces the conditional autocovariance function $K_{\bar{N}}(t_1,t_2)$ as

$$\begin{aligned} K_{\bar{N}}(t_1,t_2) = \rho^2\int_{-\infty}^{\infty}\int_{-\infty}^{\infty} & m(\omega,t_1)m^*(\omega,t_2)m^*(\omega',t_1) \\ & \times m(\omega',t_2)\exp[i(\omega-\omega')(t_1-t_2)] \\ & \times\mathrm{tr}[\hat{\mathbf{G}}(\omega)\hat{\mathbf{G}}^\dagger(\omega')]\mathrm{d}\omega\mathrm{d}\omega'. \end{aligned} \tag{35}$$

Hence the total autocovariance function is given by

$$\begin{aligned} K(t,t') = & \left(\frac{e}{\Delta t}\right)^2\int_{-\infty}^{\infty} r(t-t_1)r(t'-t_1)\langle\langle N(t_1)\rangle\rangle\mathrm{d}t_1 \\ & + \left(\frac{e}{\Delta t}\right)^2\int_{-\infty}^{\infty}\int_{-\infty}^{\infty} r(t-t_1)r(t'-t_2)K_{\bar{N}}(t_1,t_2)\mathrm{d}t_1\mathrm{d}t_2 \end{aligned} \tag{36}$$

It is shown in Appendix A that if the PSD has as large a bandwidth as required by OCI, on the order of 10^{13} Hz, the second term on the right-hand side of Eq. (36) can be neglected so that the total autocovariance function can be approximated as

$$K(t,t') \approx \left(\frac{e}{\Delta t}\right)^2\int_{-\infty}^{\infty} r(t-t_1)r(t'-t_1)\langle\langle N(t_1)\rangle\rangle\mathrm{d}t_1 \tag{37}$$

3. Specimen Model

For the sake of our assessment, a specimen model, which is described mathematically by the term $\hat{\beta}(\omega)$, will be defined as a single layer bounded by two interfaces as shown in Fig. 2. The first interface is a boundary between air and the layer refractive index n. The second interface is a boundary between the layer refractive index n and a substrate refractive index $n+\Delta n$. A distance l separates the two interfaces. The expression for the reflection from this specimen model is given in Eq. (38), with the Fresnel reflections r_1 and r_2, and the phase delay $\delta(\omega)$ given by Eq. (39).

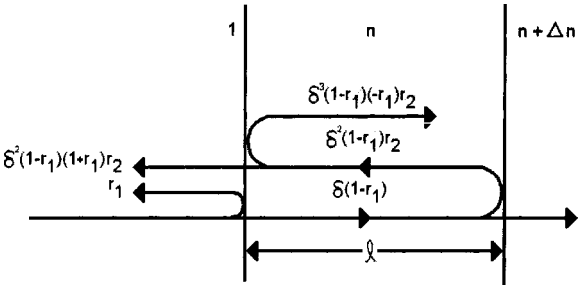

Fig. 2. Illustration of the specimen model.

$$\hat{\beta}(\omega) = r_1 + (1 - r_1^2) r_2 \delta^2(\omega), \tag{38}$$

$$r_1 = \frac{1-n}{1+n}, \qquad r_2 = \frac{-\Delta n}{2n + \Delta n}, \quad \delta(\omega) = \exp\left(i\omega \frac{nl}{c} \right). \tag{39}$$

We have ignored multiple reflections because of the low reflected power at each interface for the changes in refractive index that we will consider.

C. Task Definitions

We shall investigate two tasks for assessing the performance of the system: a detection task and a resolution task.

For the detection task, we will assess the smallest change in index of refraction at the second interface that the system can discriminate. Therefore we define the negative hypothesis H_0 as no second interface, i.e., $\Delta n = 0$. The positive hypothesis H_1 is defined as having a second interface, i.e., $\Delta n = \Delta n_0 \neq 0$. For H_1, Δn_0 will be increased so that we can see how the detectability index and the AUC vary. To be sure that reflected fields from the two interfaces of the specimen model do not interfere for this task, we set the separation distance l to be the longest coherence length of the three theoretical sources considered.

For the resolution task, we assess the smallest separation of the two interfaces of the layer that the system can discriminate. Therefore we have Δn equal to a constant. The negative hypothesis H_0 for this task is defined as the two interfaces at the same location, i.e., $l = 0$. The positive hypothesis H_1 corresponds to the two interfaces separated by a distance, i.e., $l = l_0 \neq 0$. For H_1, l_0 will be increased so that we can see how the detectability index and the AUC vary for various values of the constant Δn for each theoretical source considered.

3. SIMULATION

To properly simulate the detectability index associated with the detection task and the resolution task defined in Section 2, we must first define the theoretical setup and choose reasonable input parameters. We will consider the theoretical system to be the free-space interferometer system shown in Fig. 1. The scanning mechanism will be a mirror translating at a speed v_m. As previously stated, we will investigate the detection task and the resolution task for three theoretical Gaussian PSDs. These normalized Gaussian PSDs are defined mathematically as[11]

$$S(\omega) = \frac{2(\ln 2)^{1/2}}{\pi^{1/2} \Delta\omega} \exp\left\{ - \left[2(\ln 2)^{1/2} \frac{\omega - \omega_0}{\Delta\omega} \right]^2 \right\}, \tag{40}$$

where ω_0 is the center angular frequency and $\Delta\omega$ is the angular-frequency bandwidth (i.e., the spectral width) at FWHM. The angular-frequency bandwidth is related to the coherence length l_c of the source as

$$\Delta\omega = \frac{8 \ln 2}{l_c} c. \tag{41}$$

The resolution may be considered to be half the coherence length.[11] To define the three Gaussian PSDs, we consider coherence lengths of 2, 20, and 40 μm, corresponding to resolutions of 1, 10, and 20 μm and angular-frequency bandwidths of 8.32×10^{14} rad/s, 8.32×10^{13} rad/s, and 4.16×10^{13} rad/s. Also, we consider the center angular frequency of all of these PSDs to be 1.98×10^{15} rad/s, which corresponds to a wavelength of 950 nm. To establish the sampling frequency of the power spectrum of the source, we define the bandwidth B to be $\Delta\omega/2\pi$ expressed in hertz. The autocorrelation function that is the Fourier transform of the PSD is considered to be defined in a time range L of $3.5/B$. We define the extent of the Gaussian to be 3.5 times its sigma, given that below this value the Gaussian is very close to zero. The maximum optical frequency F of the PSD is given by $(\omega_0 + 1.75\Delta\omega)/2\pi$. According to the Nyquist sampling condition, the sampling step ΔT in the time domain should be at least $1/(2F)$. The number of samples in the PSD or its Fourier transform is then given by $L/\Delta T$. We computed that for the three values of the three coherence lengths in increasing order (i.e., 2, 20, and 40 μm) and the associated PSD, the minimum number of samples that the computation yields is 29, 179, and 346, respectively. In the simulations, each of the PSDs was sampled with 600 points over the angular frequency range of $\omega_0 - 1.75\Delta\omega$ to $\omega_0 + 1.75\Delta\omega$, which is well above the minimum required; this range minimizes sampling in the tails of each Gaussian PSD, where the PSDs have values near zero. Also, the power for each of these three theoretical sources is set to 3 mW. For ease in comparing the results, in the simulation we will vary no parameters other than the coherence length and therefore the angular-frequency bandwidth and the parameter to be varied for each task.

We must also provide quantitative parameters for the values of $\hat{\alpha}(\omega)$, $\phi_1(\omega,t)$, and $\phi_2(\omega,t)$ given in Eq. (12), the value of Δt given in Eq. (7), the values of R and A given in Eq. (16), and the value of n given in Eq. (39). The losses and phase shifts of the beam splitter are ignored, and the mirror is assumed to have a unit reflection for all frequencies: $\hat{\alpha}(\omega)$ is 1. The phase terms $\phi_1(\omega,t)$ and $\phi_2(\omega,t)$ are set to $\omega(2l_r/c) + v_m t$ and $\omega(2l_s/c)$, respectively. The constants l_r and l_s are the distances from the point where the field is split to the initial location of the reference mirror and the specimen, respectively. For the purpose of the simulation, l_s is chosen to be 3 mm, and l_r is chosen to be 3 mm less 28 μm. The speed of the mirror v_m is chosen to be 0.154 m/s, and t is increased from zero by steps of 0.4 μs over the total scan time of 0.8 ms for a total of 2000 time samples. The detector integration time Δt is 4 μs (i.e., bandwidth is 125 KHz); thus time sampling at 2.5 MHz (i.e., every 0.4 μs) ensures that the Nyquist sampling condition will be satisfied. The responsivity R of the detector is assumed to be 1 for all frequencies, and the area A of the detector is chosen to be 0.79 mm^2; these quantities result in a ρ value of 1.3097×10^{10} m^2/(V^{2}s). The value of the refractive index n is set to 1.4.

Finally, finite-width integrations, and more particularly trapezoidal numerical integrations, were performed in the simulations.

A. Detection Task

As previously stated for the detection task, we will assess the smallest change in refractive index at the second in-

terface that our system can discriminate. To be sure that the interference between the two interfaces of the specimen model does not influence this measure, we set the distance between the two interfaces l to 40 μm, the longest coherence length considered. The value of Δn_0 is then increased from 0 to 3×10^{-5}. The plots for the detectability index and the AUC versus the value of Δn_0 for each coherence length considered are given in Fig. 3.

B. Resolution Task

For the task of resolution, we assess the smallest separation of the two interfaces of the layer defined in Section 2 that the system can discriminate. To compute the detectability index and the AUC for the resolution task, we chose a change in refractive index corresponding to (a) a 75% probability of detection (AUC=0.75), (b) the smallest change in refractive index corresponding to 100% probability of detection (AUC first reaches 1), and (c) twice the smallest change in refractive index corresponding to 100% probability of detection for the detection task for each of the three coherence lengths; these three refractive indices will be denoted Δn_1, Δn_2, and Δn_3, respectively. These changes in refractive indices are $\Delta n_1=6.51\times10^{-6}$, $\Delta n_2=3\times10^{-5}$, and $\Delta n_3=6\times10^{-5}$ for a coherence length of 2 μm; $\Delta n_1=2.06\times10^{-6}$, $\Delta n_2=1.05\times10^{-5}$, and $\Delta n_3=2.1\times10^{-5}$ for a coherence length of 20 μm; and $\Delta n_1=1.45\times10^{-6}$, $\Delta n_2=9\times10^{-6}$, and $\Delta n_3=1.8\times10^{-5}$ for a coherence length of 40 μm. For each of the three coherence lengths, the value of l_0 is increased from 0 to the coherence length so we can see how the detectability index and the AUC change with the separation distance l_0. The plots for the detectability index and the AUC versus the value of l_0, the separation distance, for each of the cases are given in Fig. 4.

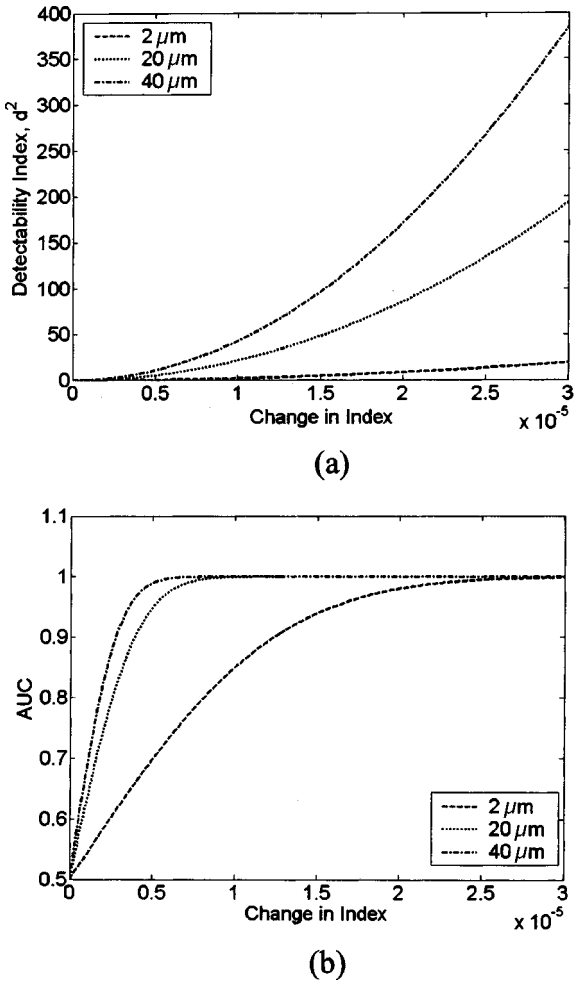

Fig. 3. Detection task. (a) Detectability index, (b) AUC for Gaussian sources of 2, 20, and 40 μm coherence length.

4. DISCUSSION

In this section we discuss the results of the simulation for both the detection task and the resolution task. Also, we reiterate the assumptions made in this paper and present the possible extensions of the mathematical framework provided.

A. Detection Task

As expected and as seen in Fig. 3, the increase in the detectability index and the AUC as a function of increasing change in refractive index signifies that it becomes easier for the observer to discriminate between a second interface and no second interface as the change in refractive index increases. Specifically, according to the plot of the AUC in Fig. 3(b), with the parameters used and the system modeled the observer can detect a second interface with 100% probability when a change in index of 3×10^{-5} occurs for a coherence length of 2 μm, 100% probability when a change in index of 1.05×10^{-5} occurs for a coherence length of 20 μm, and 100% probability when a change in index of 9×10^{-6} occurs for a coherence length of 40 μm. These three changes in refractive index constitute the benchmark performance for the detection task. Overall, a longer coherence length source has a greater detectability index for a lower change in refractive index. This phenomenon stems from the fact that under exactly the same conditions, a longer coherence length source has larger values for the **X** vector than a shorter coherence length source, as shown in Fig. 5.

B. Resolution Task

As expected and as seen in Figs. 4(d)–4(f), the AUCs increase as the separation distance between the two interfaces increases. However, within a separation distance that is less than half the coherence length of the source, oscillations are observed in both the detectability index [Figs. 4(a)–4(c)] and the AUCs [Figs. 4(d)–4(f)], at least for the smallest change in refractive index indicated in the curve definitions; these oscillations correspond to interference from fields reflected from the first and second interfaces of the specimen model. Indeed, when the separation of the two interfaces of the specimen model is smaller than half the coherence length of the source, the reflected fields from the two interfaces interfere constructively if the optical path difference between the two layers is a multiple of the central wavelength of the source. Similarly, for separations corresponding to out-of-phase interfering fields, the fields interfere destructively. As the separation increases, the contrast of the fringes decreases as a consequence of the nonmonochromatic light field. Upon first observing these oscillations, we validated that

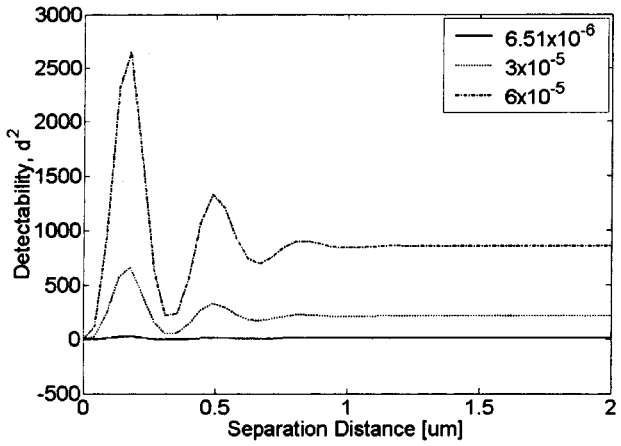

(a)

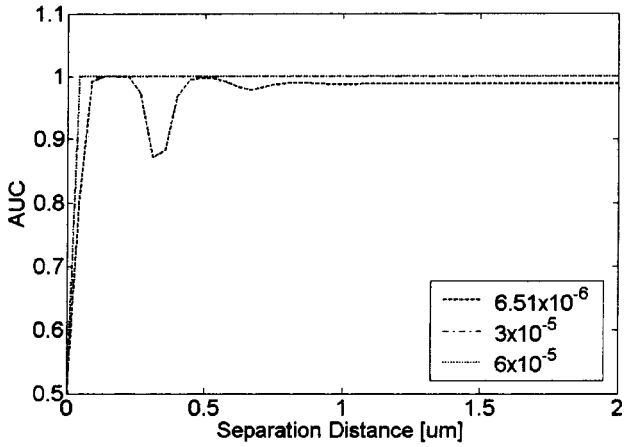

(d)

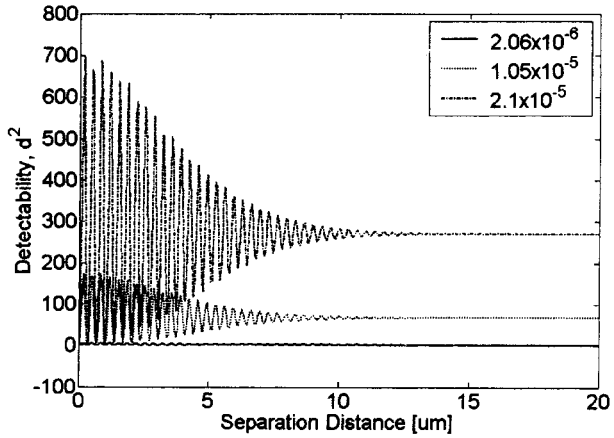

(b)

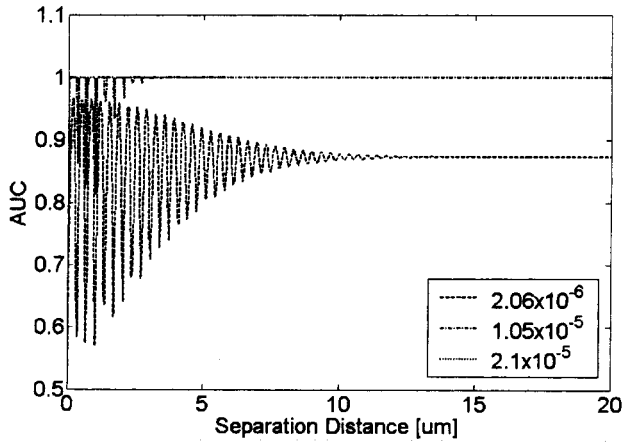

(e)

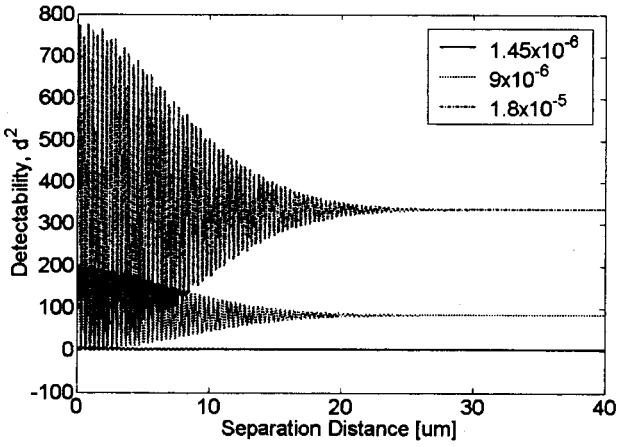

(c)

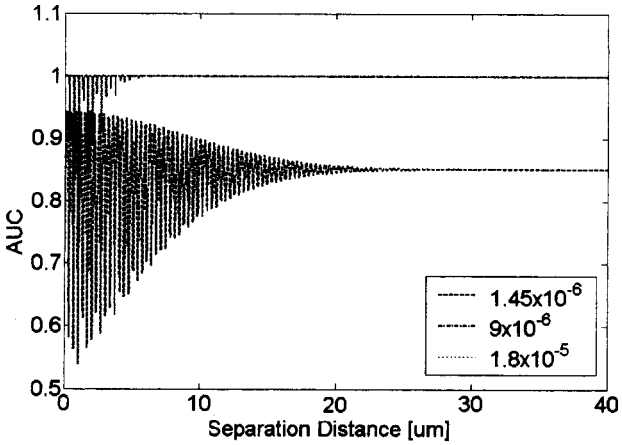

(f)

Fig. 4. Resolution task. Detectability index versus separation distance for sources with coherence length of (a) 2 μm, (b) 20 μm, and (c) 40 μm. AUC versus separation distance for sources with coherence length of (d) 2 μm, (e) 20 μm, and (f) 40 μm.

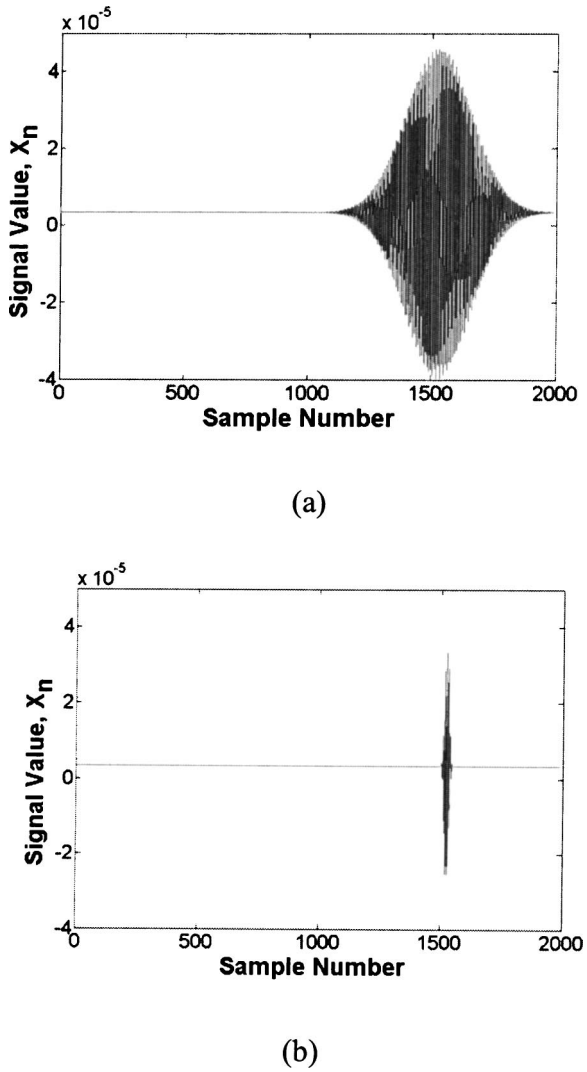

Fig. 5. Signal **X** for the detection task given $\Delta n_0 = 0.1$ for coherence length sources of (a) 40 μm and (b) 2 μm.

the oscillations' period corresponded to optical separations that are multiples of the source's central wavelength. Although this phenomenon is not speckle, since we are dealing only with two layers rather than with a scattering medium, it is reminiscent of speckle, which corresponds to multiple-scatterers' interference for interferences localized within the coherence length of the source. In practice, given a specimen with varying properties such as unequal thickness layers or slight inhomogeneities in the refractive index defining a layer, the rapid oscillations will be averaged out. Such averaging may also apply when new sources of system noise are considered. Thus we expect that in practice, these high-frequency oscillations will have no effect on system optimization.

Interestingly, even when the layer separation is beyond half the coherence length of the source, the observer can discriminate between two separated layers and two coinciding layers with only $<100\%$ probability for the smallest change in index of refraction. Also, through inspection of the AUC in Figs. 4(d)–4(f), it can be seen that for shorter coherence lengths, the resolution performance of the system depends less on the detection limit established in the detection task study; the shorter the coherence length, the higher the probability of distinguishing between two separated layers or two coinciding layers for refractive indices below the detection limit determined by the detection task. Thus the resolution performance of the system depends on both the broadband source and the specimen being imaged.

For the change in refractive index Δn_3, while the detectability index has the same general behavior as the change in refractive indices Δn_1 and Δn_2, it can be seen that the AUC has changed tremendously. In fact, the AUC shows that for any separation distance greater than zero, the observer can discriminate between two separated layers and two coinciding layers with 100% probability. This finding is in agreement with the following statement by Harris[12]:

"In the classic case of resolving two point sources in the presence of Gaussian noise, results indicate that although diffraction increases the difficulty of rendering a correct binary decision, it does not prevent a correct binary decision from being made, no matter how closely spaced the two point sources may be" (p. 611).

Although this statement concerns incoherent imaging, it is easily extended to the case of two layers in OCI. Therefore for a sufficient change in refractive index at the second interface, there is a 100% probability of distinguishing between two separated layers and two coinciding layers. This sufficient change in refractive index is approximately Δn_3. Thus for each of the three theoretical sources, the resolution benchmark is 100% probability of discrimination of two separated layers from two coinciding layers for $\Delta n \geq \Delta n_3$ for the corresponding source regardless of l_0. This finding is further supported by previous observation by Richards-Kortum and associates, who state that "changes in scattering occur on a microscopic spatial scale well below the typical resolution of OCT imaging systems, yet these changes still impact OCT images" (Ref. 13, p. 465).

C. Assumptions and Possibilities

Although the mathematics for the mean and autocovariance of the photocurrent output of the OCI system were derived for the simple case of unpolarized light, an isotropic specimen model, and normal incidence of the propagating beam, these derivations can be extended to include polarization dependence, a nonisotropic specimen, and nonnormal incidence. We will include these cases as part of future work.

The three PSDs considered within this paper are all the commonly used Gaussian shapes. However, the mathematical framework provided allows for any arbitrary PSD to be used. We have done precisely this in a previously published study.[14]

Furthermore, the demonstrated system did not include any noise other than the Gaussian noise from the source and the Poisson noise of the detection process; this system was simulated in order to verify that the model behaves as expected. This model provides the basic framework for which inclusion of more-realistic system components and other sources of noise can be carried out for any general

OCI system. Also, the benchmark performance introduced is set forth so that in the future, the results obtained with more-complex models can be compared with the results of the simple OCI system modeled in the current study.

5. CONCLUSION

We have presented the basics of a model to optimize and assess the performance of a general OCI system based on the basis of task performance and statistical decision theory. This general model was adapted to a simple OCI system to allow us to assess the performance of the system in terms of a specific detection task and a specific resolution task.

For a task-based performance assessment on the detection task for the simple OCI system presented, the smallest change in refractive index detectable was shown to be dependent on the angular-frequency bandwidth of the source. Considering the system parameters, a benchmark performance for the detection task is that a change in refractive index of 3×10^{-5} is detectable for a Gaussian source of 2 μm coherence length, a change in refractive index of 1.05×10^{-5} is detectable for a Gaussian source of 20 μm coherence length, and a change in refractive index of 9×10^{-6} is detectable for a Gaussian source of 40 μm coherence length, with 100% probability.

Furthermore, the performance of this system based on the resolution task was shown to be dependent on the specimen model and the angular-frequency bandwidth of the source for small changes in the refractive index at the second interface. Also, the performance of the system based on the resolution task for changes in refractive index well beyond the detection limit was seen to agree with previous findings. This agreement is that for infinitely close interfaces of sufficient change in index, i.e., changes well beyond the detection limit of 100%, the binary classification task of whether there are two separated layers or two coinciding layers can be carried out with 100% accuracy.

APPENDIX A

By performing order-of-magnitude estimation, we will show that the Poisson statistics' contribution to the autocovariance dominates the Gaussian statistics' contribution to the autocovariance. The Gaussian statistics' contribution to the autocovariance of the photocurrent can be written as

$$K_G(t,t') = \left(\frac{e}{\Delta t}\right)^2 \int_{-\infty}^{\infty}\int_{-\infty}^{\infty} r(t-t_1)r(t'-t_2)K_{\bar{N}}(t_1,t_2)\mathrm{d}t_1\mathrm{d}t_2, \tag{A1}$$

where

$$K_{\bar{N}}(t_1,t_2) = \rho^2 \int_{-\infty}^{\infty}\int_{-\infty}^{\infty} m(\omega,t_1)m^*(\omega,t_2)m^*(\omega',t_1)m(\omega',t_2) \times \exp[i(\omega-\omega')(t_1-t_2)]\mathrm{tr}[\hat{\mathbf{G}}(\omega)\hat{\mathbf{G}}^\dagger(\omega')]\mathrm{d}\omega\mathrm{d}\omega'. \tag{A2}$$

The term $m(\omega,t)$ is defined as

$$m(\omega,t) = \hat{\alpha}(\omega)\exp[i\phi_1(\omega,t)] + \hat{\beta}(\omega)\exp[i\phi_2(\omega,t)] = C_1(\omega,t) + C_2(\omega,t). \tag{A3}$$

The term $\mathrm{tr}[\hat{\mathbf{G}}(\omega)\hat{\mathbf{G}}^\dagger(\omega')]$ can be expanded as

$$\mathrm{tr}[\hat{\mathbf{G}}(\omega)\hat{\mathbf{G}}^\dagger(\omega')] = \hat{G}_{xx}(\omega)\hat{G}^*_{xx}(\omega') + \hat{G}_{xy}(\omega)\hat{G}^*_{yx}(\omega') + \hat{G}_{yx}(\omega)\hat{G}^*_{xy}(\omega') + \hat{G}_{yy}(\omega)\hat{G}^*_{yy}(\omega') = \sum_{m=1}^{2}\sum_{n=1}^{2}\hat{G}_{mn}(\omega)\hat{G}^*_{mn}(\omega'), \quad x=1, \quad y=2. \tag{A4}$$

Using the definition in Eq. (A3) and the expansion in Eq. (A4), Eq. (A2) can be rewritten as

$$K_{\bar{N}}(t_1,t_2) = \rho^2 \sum_{h=1}^{2}\sum_{j=1}^{2}\sum_{k=1}^{2}\sum_{l=1}^{2}\sum_{m=1}^{2}\sum_{n=1}^{2}\int_{-\infty}^{\infty} C_h(\omega,t_1)C^*_j(\omega,t_2) \times \exp[i\omega(t_1-t_2)]\hat{G}_{mn}(\omega)\mathrm{d}\omega \times \int_{-\infty}^{\infty} C^*_k(\omega',t_1)C_1(\omega',t_2)\exp[-i\omega'(t_1-t_2)] \times \hat{G}^*_{mn}(\omega')\mathrm{d}\omega'. \tag{A5}$$

Equation (A5) has a total of 64 terms. The two integration terms are Fourier transforms of the composite functions $C_h(\omega,t_1)C^*_j(\omega,t_2)\hat{G}_{mn}(\omega)$ and $C^*_k(\omega',t_1)C_l(\omega',t_2)\hat{G}^*_{mn}(\omega')$; we are concerned with the behavior of these autocovariance terms only in terms of the difference between t_1 and t_2. If we assume that the functions $\hat{\alpha}(\omega)$ and $\hat{\beta}(\omega)$ have very broad spectral responses, i.e., the spectral responses of these functions are much greater than the bandwidth of the PSDs represented by $\hat{G}_{mn}(\omega)$, and that the phase functions $\phi_1(\omega,t)$ and $\phi_2(\omega,t)$ are real, these Fourier transform terms will have widths in the time (t_1-t_2) domain on the order of the inverse of the frequency bandwidth of the PSDs. Also, by the central ordinate theorem, these terms will have a peak value proportional to the integral of the PSDs. We will not concern ourselves with the integrations in time in Eq. (A1). These integrations will serve only to smooth the autocovariance.

If we use angular-frequency bandwidths of the PSDs on the order of $2\pi\times10^{13}$ rad/s, the Fourier transform has a width in the time domain on the order of 1×10^{-13} s. Assuming a normalized area of 1 for the PSDs for ease and using the value of 1×10^{10} m^2/(V^{2}s) for ρ, we can consider the autocovariance as an equivalent delta function with

$$K_{\bar{N}}(t_1,t_2) = \underline{O}[6.4\times10^{-5}\delta(t_1-t_2)], \tag{A6}$$

where $\underline{O}$ represents "on the order of."

The autocovariance term of the Poisson statistics $\langle N(t_1)\rangle\delta(t_1-t_2)$, with the same broad approximations, is equivalently

$$\langle\langle N(t_1)\rangle\rangle\delta(t_1-t_2) = \underline{O}[1\times10^{10}\delta(t_1-t_2)]. \tag{A7}$$

Thus the Gaussian statistics' contribution to the autocovariance can be considered negligible in comparison with that of the Poisson statistics.

ACKNOWLEDGMENTS

We thank Harry Barrett and Kyle Myers for stimulating discussion about this work. This work was supported in part by National Cancer Institute Contract CA87017, National Science Foundation Division of Information and Intelligent Systems grant 00-82016, the Division of Information Technology Research, the U.S. Army Research Office, the University of Central Florida Presidential Instrumentation Initiative, the Defense Advanced Research Projects Agency, the National Science Foundation Procurement Technical Assistance Program, and the Florida Photonics Center of Excellence.

Corresponding author Jannick Rolland's e-mail address is jannick@odalab.ucf.edu.

REFERENCES

1. D. Huang, E. A. Swanson, C. P. Lin, J. S. Schuman, W. G. Stinson, W. Chang, M. R. Hee, T. Flotte, K. Gregory, C. A. Puliafito, and J. G. Fujimoto, "Optical coherence tomography," Science **254**(5035), 1178–1181 (1991).
2. A. F. Fercher, W. Drexler, C. K. Hitzenberger, and T. Lasser, "Optical coherence tomography—principles and applications," Rep. Prog. Phys. **66**, 239–303 (2003).
3. J. M. Schmitt, "Optical coherence tomography (OCT): a review," IEEE J. Sel. Top. Quantum Electron. **5**, 1205–1215 (1999).
4. H. H. Barrett and K. J. Myers, "Image quality," in *Foundations of Image Science*, Series in Pure and Applied Optics (Wiley, Hoboken, New Jersey, 2004), Chap. 14, pp. 913-1000.
5. M. A. Kupinski, J. W. Hoppin, E. Clarkson, and H. H. Barrett, "Ideal-observer computation in medical imaging with use of Markov-chain Monte Carlo techniques," J. Opt. Soc. Am. A **20**, 430–438 (2003).
6. E. Clarkson and H. H. Barrett, "Approximation to ideal-observer performance on signal-detection tasks," Appl. Opt. **39**, 1783–1793 (2000).
7. W. E. Smith and H. H. Barrett, "Hotelling trace criterion as a figure of merit for the optimization of imaging systems," J. Opt. Soc. Am. A **3**, 717–725 (1986).
8. P. Bonetto, J. Qi, and R. M. Leahy, "Covariance approximation for fast and accurate computation of channelized Hotelling observer statistics," IEEE Trans. Nucl. Sci. **47**, 1567–1572 (2000).
9. H. Hotelling, "The generalization of Student's ratio," Ann. Math. Stat. **2**, 360–378 (1931).
10. J. W. Goodman, *Statistical Optics* (Wiley, New York, 2000).
11. C. Akcay, P. Parrein, and J. P. Rolland, "Estimation of longitudinal resolution in optical coherence imaging," Appl. Opt. **41**, 5256–5262 (2002).
12. J. L. Harris, "Resolving power and decision theory," J. Opt. Soc. Am. **54**, 606–611 (1964).
13. B. E. Bouma and G. J. Tearney, eds., *Handbook of Optical Coherence Tomography* (Marcel Dekker, New York, 2002).
14. J. P. Rolland, J. O'Daniel, E. Clarkson, K. Cheong, C. A. Akcay, P. Parrein, T. DeLemos, and K. S. Lee, "AUC-based resolution quantification in optical coherence tomography," in *Medical Imaging: Image Perception, Observer Performance and Technology Assessment*, D. P. Chakraborty and M. P. Eckstein, eds., Proc. SPIE **5372**, 334–353 (2004).